Graphical Abstract

Temporal Evolution of Lift in a Pure Cruciform System for Energy Harvesting

Ahmad Adzlan,Mohamed Sukri Mat Ali,Sheikh Ahmad Zaki Shaikh Salim

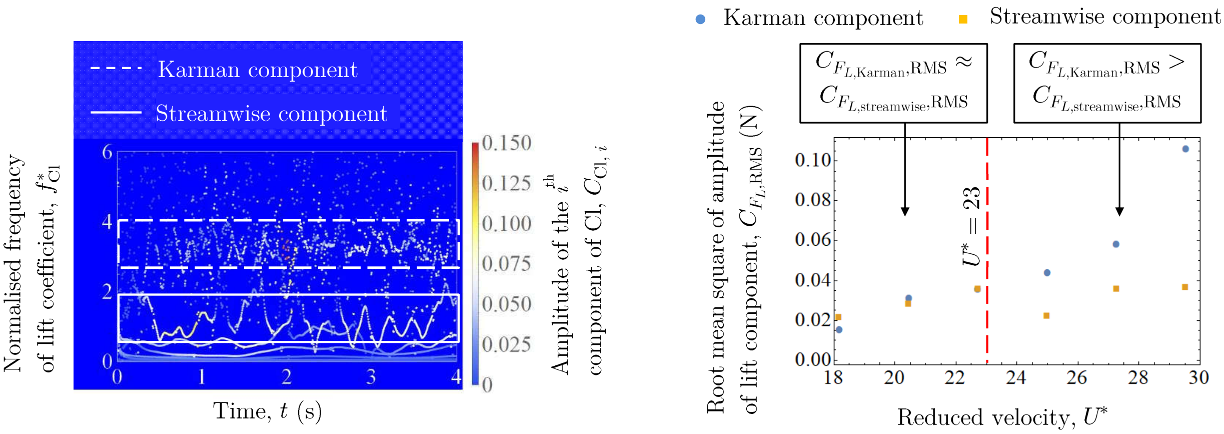

Highlights

Temporal Evolution of Lift in a Pure Cruciform System for Energy Harvesting

Ahmad Adzlan,Mohamed Sukri Mat Ali,Sheikh Ahmad Zaki Shaikh Salim

- Decomposition of the lift coefficient signal via ensemble empirical mode decomposition (EEMD) brings to the fore the components of lift generated by the shedding of Karman and streamwise vortices, which in its original form is observed as one non-monotonic lift signal in the streamwise vortex-induced vibration (SVIV) regime.
- Determination of phase lag between lift and cylinder displacement using Hilbert-Huang Transform (HHT) reveals evidence suggesting the existence of an initial branch for SVIV.
- Contribution to the total root-mean-square (RMS) lift amplitude from the shedding of both Karman and streamwise vortices suggest that we might be able to enlarge the RMS amplitude – and as a result harnessed power – if we can redirect energy away from Karman vortices towards streamwise vortices, in the SVIV regime.

Temporal Evolution of Lift in a Pure Cruciform System for Energy Harvesting

Ahmad Adzlan[a,b,*], Mohamed Sukri Mat Ali[a] and Sheikh Ahmad Zaki Shaikh Salim[a]

[a]Malaysia-Japan International Institute of Technology, Universiti Teknologi Malaysia, 54200 Kuala Lumpur, Malaysia
[b]Faculty of Engineering, Universiti Malaysia Sarawak, 94300 Kota Samarahan, Sarawak, Malaysia

ARTICLE INFO

Keywords:
Vortex-induced vibration
Vibration energy harvester
CFD simulation
Streamwise vorticity
Ensemble empirical mode decomposition (EEMD)
Hilbert transform

ABSTRACT

We investigated the amplitude and frequency responses of a circular cylinder - strip plate cruciform system in the Reynolds number range $1.1 \times 10^3 < Re < 14.6 \times 10^3$ numerically using the open source C++ library: OpenFOAM. We decomposed the cylinder displacement and lift time series from our numerical results into Hilbert transform-friendly signals using the ensemble empirical mode decomposition (EEMD) method. The mean phase lag obtained through Hilbert transform points to the existence of an initial branch-like state, with a phase lag of ≈ 20 deg. in the narrow region of U^* close to 18.2. Then, the mean phase lag jumps from ≈ 20 deg. to ≈ 110 deg. once U^* reaches 20.5, analogous to the transition to upper branch in a KVIV amplitude response curve. The instantaneous phase lag shows that SVIV is quasi-periodic up until $U^* = 27.3$. Between $18.2 < U^* < 22.5$, Karman vortex shedding contributes nearly as much as streamwise vortex shedding to the root-mean-square amplitude of total lift, while between $25.0 \leq U^* \leq 29.5$, the Karman component contribution is on average twice that of the streamwise component. These findings hint at the possibility to improve the power output of the harvester by a factor of two between $18.28 < U^* < 22.5$ and by a factor of three between $25.0 \leq U^* \leq 29.5$, if we can unite the contribution to the root-mean-square amplitude of the total lift under a single vibration-driving mechanism: the shedding of streamwise vortex.

1. Introduction

Streamwise vortex-induced vibration (SVIV) is a type of vortex-induced vibration (VIV) driven by vortical structures whose vorticity vector points in the direction of the free stream. In recent decades, there have been efforts to exploit the SVIV phenomenon from cruciform structures for energy harvesting. The literature on this subject can be broadly categorised into two groups: how the mechanical properties of the oscillator (e.g., mass ratio, damping, etc.) affects the amplitude/frequency response of SVIV (Koide et al., 2009, 2013; Nguyen et al., 2012) and how the minutiae of the flow field affect the force driving the vibration of the cylinder, i.e. the fluid mechanical aspect of the system (Deng et al., 2007; Koide et al., 2017; Zhao and Lu, 2018).

In the first focus area, researchers studied some permutation of the following method to convert the vibration into electrical power. The method consists of a coil and magnet. The coil, which moves with the vibrating cylinder, creates relative motion against the magnet, which is placed in the hollow of the coil (Koide et al., 2009). While investigating the system at a Reynolds number in the order of Re $\sim O\left(10^4\right)$, Koide et al. (2009) showed that increased damping due to energy harvesting reduces the maximum vibration amplitude close to a factor of 4. Amplitude reduction due to

*Corresponding author
aafkhairi@graduate.utm.my (A. Adzlan); sukri.kl@utm.my (M.S.M. Ali); sheikh.kl@utm.my (S.A.Z.S. Salim)
ORCID(s): 0000-0003-0290-3185 (A. Adzlan)

increased total damping was also mentioned in Bernitsas et al. (2008); Bernitsas and Raghavan (2008); Bernitsas et al. (2009). Further investigation in Nguyen et al. (2012) revealed that damping not only affects the amplitude response of the cylinder but also narrows the synchronisation region between vortex shedding and cylinder vibration. Moreover, Nguyen et al. (2012) demonstrated a strong coupling between mass ratio and damping in determining both the width of the synchronisation region and the maximum amplitude response of the cylinder.

In the second focus area, investigators turned their attention to the details of the flow where streamwise vortex shedding occurs. One such study carefully shot motion pictures of the dye-injected flow (Koide et al., 2017) at Reynolds number in the order of $\mathrm{Re} \sim O\left(10^3\right)$. A lower Reynolds number (Re) reduces the amount of turbulence in the flow, allowing a clearer shot of the vortex structures. Their study also highlights the higher level of turbulence produced by the circular cylinder—strip-plate cruciform in contrast to the twin circular cylinder cruciform, which diminishes the periodicity of vortex shedding. Although visually enlightening, this and other more qualitative studies contribute little towards improving our understanding of the relationship between vortex shedding and the resulting lift. Deng et al. (2007) demonstrated a way to overcome such a shortcoming.

In their study, Deng et al. (2007) examined the flow field of a twin circular cylinder cruciform using computational fluid dynamics (CFD). Their domain stretches $28D$ in the streamwise direction, $16D$ in the transverse direction and $12D$ in the spanwise direction. They studied an Re range yet another order of magnitude smaller than that studied by Koide et al. (2017), possibly to get an even clearer visualisation of the vortical structures with less turbulence, and to ease computational requisites.

At a fixed $\mathrm{Re} = 150$, streamwise vortices form even at a gap ratio of 2. This result differs quite strikingly from Koide et al. (2006, 2007), conducted at an Re twice the order of magnitude of Deng et al. (2007), an indication that the minimum gap ratio needed for the onset of streamwise varies with respect to Re.

They also observed that when the gap ratio G, which they denote as L/D in their paper, increases from 3 to 4, the maximum amplitude of the lift coefficient increases by almost threefold. This can be attributed quite easily to the current vortex pair shed by the upstream cylinder. The downstream cylinder immediately disturbs the pair shed from the upstream cylinder when $G = 3$. The lift coefficient increases by about a factor of 3 when this immediate disturbance diminishes at $G = 4$. The visualisation of three-dimensional (3D) vorticity isocontours enables us to quickly establish this link vis-à-vis the lift coefficient signal. The authors use of CFD made this possible.

A similar study in the order of magnitude $\mathrm{Re} \sim O\left(10^2\right)$ by Zhao and Lu (2018) particularly highlighted the immense utility of CFD as a tool to research SVIV or flow around a cruciform in general. They computed the sectional lift coefficient along the upstream cylinder and the time history of this sectional lift coefficient points towards two different modes of vortex shedding, namely, parallel and K-shaped. They also paid attention to the local flow patterns that vary along the length of the upstream cylinder such as the trailing vortex flow, necklace vortex flow and flow in

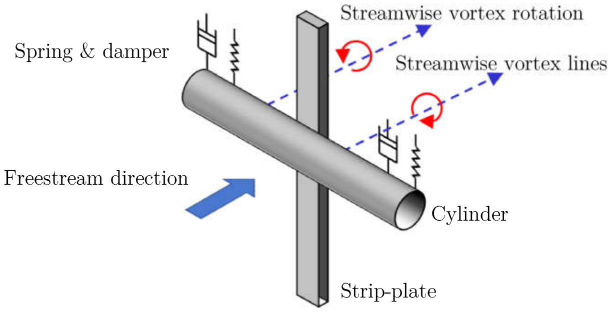

Figure 1: A schematic of the circular cylinder-strip plate cruciform system. Alternate shedding of the steamwise vortices create the alternating lift that drives the vibration of the cylinder.

the small gap (denoted as SG flow). As shown by the discontinuities in the phase angle of the sectional lift coefficient along the upstream cylinder, we wondered whether the lift coefficient here can be considered due to streamwise vortex shedding alone, when Karman vortex streamlines were also observed some distance away from the junction of the cruciform.

While we find in persuasive to attribute the frequency/ amplitude modulation of the lift signal in a KVIV system to the shedding of Karman vortices, one becomes more cautious in doing to the same solely as the result of streamwise vortex shedding in an SVIV system. The main reason behind this lies in the fact that the cylinder continues to shed Karman vortices even after the onset for streamwise vortex shedding and SVIV (Shirakashi et al., 1989). This point leads us to hypothesise that the lift signal is more appropriately viewed as the streamwise-Karman vortex-induced composite lift signal. However, we could not find studies that took this viewpoint in their investigation of SVIV and worked out its implication on power generation.

The objectives of this study are thus threefold: (1) to take a closer look at the amplitude and frequency response of a circular cylinder-strip plate cruciform, especially in U^* ranges where the transition from KVIV to SVIV occurs, (2) to demonstrate the compositeness of the lift signal of an SVIV system and establish the difference between the lift signal characteristics in the KVIV and SVIV regime and (3) to shed light on how the contribution from the Karman and streamwise components of lift changes as we increase U^* after the onset of SVIV and predict how much improvement in the power generation can be anticipated if we are able to unify the lift amplitude contributions due to Karman and streamwise vortex shedding. The following §2 details the methodology we employ to conduct this study. We present and discuss our results in §4, §5, and §6. We describe our conclusions in §7.

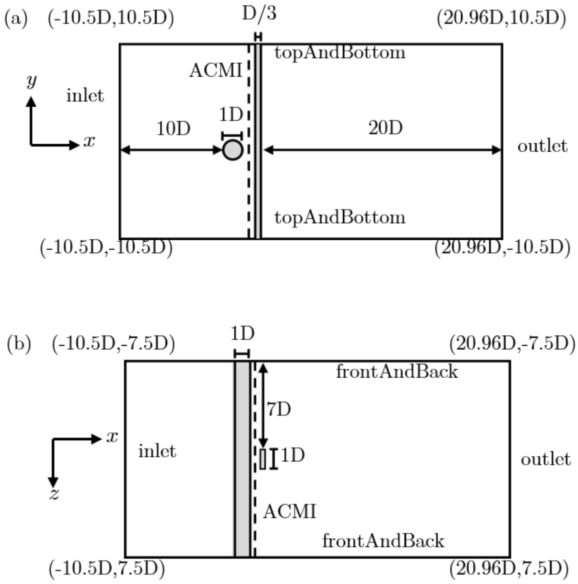

Figure 2: Problem geometry and coordinate system used. (a) shows the side view of the simulation domain (viewed parallel to the freestream) while (b) shows the top view of the simulation domain (viewed perpendicular to the freestream). Note that the gap ratio G between the cylinder and the strip plate is $0.16D$, and the ACMI patch is located midway through the gap, i.e., $0.08D$ downstream from the trailing edge of the cylinder.

2. Methodology

2.1. Problem geometry

The geometrical setup for this study builds on the work of Maruai et al. (2017, 2018) who studied both experimentaly and numerically the FIM of a square cylinder with a downsteam flate plate. Their simulation results are in good agreement with their own experiment, and with the experimental results of Kawabata et al. (2013), in the Reynolds number range $3.6 \times 10^3 < \mathrm{Re} < 12.5 \times 10^3$. This is well within the Reynolds number studied in this work, i.e. $1.1 \times 10^3 < \mathrm{Re} < 14.6 \times 10^3$.

Our $x - y$ plane fundamentally follows the dimensions used in Maruai et al. (2017, 2018), except for the cylinder shape, which in this study is circular, and the $20D$ distance to the outlet is measured from the downstream face of the strip-plate. This is shown in Fig. 2. We chose the cylinder-plate gap G to be $0.26D$, as previous works have shown this gap size sustains the highest SVIV amplitude over the widest range of U^*, in comparison to other gap sizes.

As the problem geometry is explicitly three-dimensional (3D), the $x - y$ plane is extruded in the z direction, thus obtaining a 3D domain. As can be seen in Fig. 2, the circular cylinder extends from $z/D = 7.5$ to $z/D = -7.5$, while the strip-plate extends from -10.5 to $y/D = 10.5$. The $z-$direction extent is set as $z/D = \pm 7.5$ is already more than twice the spanwise reach of the streamwise vortex, thus sufficient for the vortices to materialise in our numerical solution. To compare, the spanwise extent of the numerical study by Deng et al. (2007), is $z/D = \pm 6$ and the spanwise extents of experiments by Nguyen et al. (2012) and Koide et al. (2013) are $z/D = \pm 5$.

2.2. Numerical method

The objectives of our study necessitate the solution of the continuity, and 3D unsteady Reynolds averaged Navier-Stokes (3D URANS) equations. We achieve this by using OpenFOAM, an open-source computational fluid dynamics (CFD) platform written in C++. Specifically, we work to solve the following continuity and URANS equations.

$$\frac{\partial U_i}{\partial x_i} = 0, \tag{1}$$

$$\frac{\partial U_i}{\partial t} + U_j \frac{\partial U_i}{\partial x_j} = -\frac{1}{p}\frac{P}{x_i} + \frac{\partial}{\partial x_j}\left(2\nu S_{ij} - \overline{u'_j u'_i}\right). \tag{2}$$

The symbols U, x, t, ρ, P, ν, S, and u' are the mean component of velocity, spatial component, time density, pressure, kinematic viscosity, mean strain rate and the fluctuating component of velocity, respectively. The mean strain rate S_{ij} is given by

$$S_{ij} = \frac{1}{2}\left(\frac{\partial U_i}{\partial x_j} + \frac{\partial U_j}{\partial x_i}\right). \tag{3}$$

This study employs the Spalart-Allmaras turbulence model to approximate the Reynolds stress tensor $\tau_{ij} = \overline{u'_j u' i}$. This turbulence model has been shown to produce results that agree reasonably well with experiments in similar flow-induced motion (FIM) studies (Ding et al., 2015a,b). We use the Boussinesq approximation to relate the Reynolds stress tensor to the mean velocity gradient

$$\tau_{ij} = 2\nu_T S_{ij}, \tag{4}$$

where ν_T represents the kinetic eddy viscosity. ν_T is, in turn, a function of $\tilde{\nu}$ and f_{v1}, while f_{v1} is a function of χ and c_{v1}, and χ a function of $\tilde{\nu}$ and ν, as shown in Eq. 5.

$$\nu_T = \tilde{\nu} f_{v1}, \tag{5a}$$

$$f_{v1} = \frac{\chi^3}{\chi^3 + c_{v1}^3}, \tag{5b}$$

$$\chi = \frac{\tilde{\nu}}{\nu}. \tag{5c}$$

Here, $\tilde{\nu}$ serves to mediate the turbulence model and dictates how $\tilde{\nu}$ is conserved.

$$\frac{\partial \tilde{\nu}}{\partial t} + U_j \frac{\partial \tilde{\nu}}{\partial x_j} = c_{b1}\tilde{S}\tilde{\nu} - c_{w1} f_w \left(\frac{\tilde{\nu}}{D}\right)^2 + \frac{1}{\sigma}\left\{\frac{\partial}{\partial x_j}\left[(\nu + \tilde{\nu})\frac{\partial \tilde{\nu}}{\partial x_j}\right] c_{b2} \frac{\partial \tilde{\nu}}{\partial x_i}\frac{\partial \tilde{\nu}}{\partial x_i}\right\} \tag{6}$$

c_{b1}, c_{b2}, and c_{v1} are constant with values 0.1335, 0.622 and 7.1 respectively. c_{w1} is given by

$$c_{w1} = \frac{c_{b1}}{\kappa} + \frac{1 + c_{b2}}{\sigma}, \tag{7}$$

where additional constants κ and σ are 0.41 and 2/3 respectively. f_w, on the other hand, is given by

$$f_w = g\left(\frac{1 + c_{w3}^6}{g^6 + c_{w3}}\right)^{\frac{1}{6}}. \tag{8}$$

Here, $c_{w3} = 2$ while g is given by

$$g = r + c_{w2}\left(r^6 - r\right), \tag{9}$$

where r is

$$r = \min\left(\frac{\tilde{\nu}}{\tilde{S}\kappa^2 d^2}, 10\right), \tag{10}$$

Additionally, $\tilde{S}$ is

$$\tilde{S} = \Omega + \frac{\tilde{\nu}}{\kappa^2 d^2} f_{v2}, \tag{11}$$

where Ω and d are the magnitude of vorticity and the distance from the mesh nodes to the nearest wall, respectively. Finally, f_{v2} is

$$f_{v2} = 1 - \frac{\chi}{1 + \chi f_{v1}}. \tag{12}$$

We solve these equations numerically using the PIMPLE algorithm, which combines the transient solver PISO with the steady-state solver SIMPLE for improved numerical stability.

2.3. Dynamic mesh motion

In this study, the cylinder in VIV moves perpendicular to the free stream direction. The motion unavoidably distorts the mesh around it, degrading important mesh metrics such as non-orthogonality and skewness. However, we can diffuse the mesh deformation to the neighbouring nodes as per the following Laplace equation,

$$\nabla \cdot (\gamma \nabla u) = 0. \tag{13}$$

Here, u represents the mesh deformation velocity and γ is displacement diffusion. We chose $\gamma = 1/l^2$, where l is the cell centre distance to the nearest cylinder edges. We implement the GAMG linear solver with the Gauss-Seidel smoother to solve Eq. 13. The dynamic mesh algorithm then updates the mesh node positions according to the following equation.

$$x_{\text{new}} = x_{\text{old}} + u\Delta t \tag{14}$$

The solver resumes the solution of Eqs. 1 and 2 once the mesh node positions are updated.

Another dynamic mesh handling technique used in this study is the arbitrarily coupled mesh interface (ACMI) that allows non-conforming meshes to slide over another, thus preserving the mesh quality around a moving object. The tiny gap between the cylinder and strip-plate, limits our ability to diffuse the mesh deformation to the surrounding space. ACMI is thus implemented at the centre of the gap between the circular cylinder and the strip-plate, as shown in

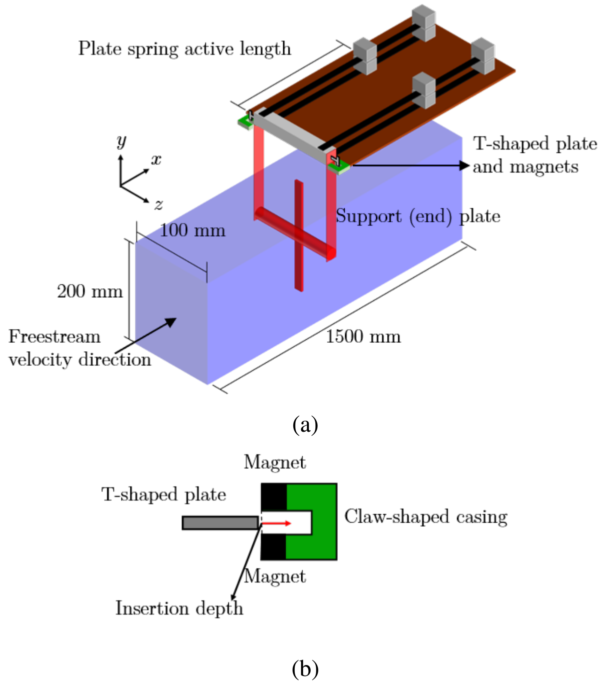

Figure 3: A schematic of our experimental setup. Fig. 3a presents a 3D schematic of the experimental rig while Fig. 3b shows an enlarged schematic of the damping system.

Fig. 2, to circumvent this problem. This method has been successfully implemented in the works of Ding et al. (2015b); Zhang et al. (2018), preserving the quality of their mesh and controlling their Courant-Friedrichs-Lewy (CFL) number.

2.4. Open flow chanel experiment

We set up an experimental rig to validate our numerical results in the vicinity of reduced velocity $U^* = 22.7$. Here, $U^* = U/f_n D$, with U, f_n and D being the freestream velocity, natural frequency of the system and the diameter of the circular cylinder respectively. We chose $U^* = 22.7$ because that value of U^* is where the vibration-driving mechanism is known to transit from Karman to streamwise vortex shedding (Koide et al., 2013). The experimental rig consists of a closed-loop open channel circuit based on the water tunnel used by Nguyen et al. (2012), shown in Fig. 3. The cross-section of our test section is a square with sides 100 mm in length. The test section is 1500 mm long.

The system for providing elastic support and damping to the circular cylinder follows closely those used by Kawabata et al. (2013) and Koide et al. (2013, 2017), which can be summarised as follows. The stiffness coefficient k of the plate spring is determined through a simple weight versus displacement test (Sun et al., 2016), at various active lengths of the spring. This provides a calibration curve of stiffness coefficient, k against plate spring length, l. We can then adjust the length of the plate spring to obtain the desired value for k.

On the other hand, the damping of the system is adjusted using T-shaped aluminium plates fixed at either end of the cylinder endplate, and a pair of neodymium magnets contained in a claw-shaped casing. The further the T-shaped

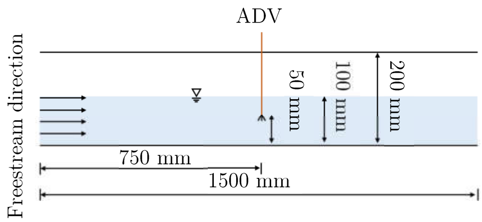

Figure 4: Side view of the open flow channel, in schematic form. Also, key dimensions of the experimental setup. The acoustic Doppler velocimeter (ADV) is placed at the same location where the cylinder is located during experimental runs.

plate is pushed into the opening of the claw, the denser the magnetic field it needs to cut through during motion, thus dissipating more energy. We then calibrate the damping produced at various depths at which the T-shaped plate is pushed into the casing, via free-decay tests of the cylinder in still water. The procedure for conducting free-decay tests are detailed in Raghavan (2007).

Flow inside the open channel is driven by a 3.728 kW (5 hp) centrifugal pump, controlled using a voltage controller. The input voltage for the centrifugal pump is calibrated against the centreline velocity of the test section, 750 mm from the inlet, i.e. mid-length of the test section. We show this schematically in Fig. 4. Here, we define the centreline of the test section as the line 50 mm from the bottom and 50 mm from either of the sidewalls of the test section. We placed the cylinder in the same position during experimental runs.

The centreline velocity $U_{\text{cent.}}$ is measured using an acounstic Doppler velocimeter (ADV), sampling at 200 Hz. The resulting calibration curve is applicable for detemining $U_{\text{cent.}}$ at input voltages $30 < V_{\text{in}}(\text{V}) < 100$. We measured the turbulence intensity along the centreline to be about 5%.

We obtained the time history for cylinder displacement, y, by using a video camera pointed normal to the cylinder endplate. We placed a visual marker on the endplate, and the motion of the marker captured by the camera is analysed using *Tracker*: a motion analysis tool built on the Open Source Physics Java framework.

To validate our experimental setup, we tuned to the best of our ability our experimental parameters to the values used by Koide et al. (2013) and test whether we can replicate their results. Table 1 summarises the parameters in lieu of that paper.

We show a sample of the normalised displacement – $y^* = y/D$ – time series in Fig. 5. Computing the statistics of y^* and the normalised cylinder vibration frequency, $f^* = f_{\text{cyl.}}/f_n$ ($f_{\text{cyl.}}$ being the vibration frequency of the cylinder), from several runs gave us a value of $y^* = 0.33 \pm 0.03$ and $f^* = 1.03 \pm 0.04$. Koide et al. (2013) obtained $y^* = 0.32$ and $f^* = 1.09$ under a similar U^* condition. We thus take this fairly successful reproduction of the results of Koide et al. (2013) as an indication of readiness for further data collection.

Table 1
Summary of experimental parameters in contrast to those used in the experimental work of Koide et al. (2013).

	Current study	Koide et al. (2013)
Cylinder diameter, D (m)	0.01	0.01
Cylinder length, l_{cylinder} (m)	0.09	0.098
Strip-plate width (m)	0.01	0.01
Strip-plate length (m)	0.1	0.1
Effective mass, $m_{\text{eff.}}$ (kg)	0.162	0.174
Logarithmic damping, δ	0.178	0.24
Scruton number, Sc	9.94	7.74
System natural frequency, f_n (Hz)	4.42	4.4 to 4.79

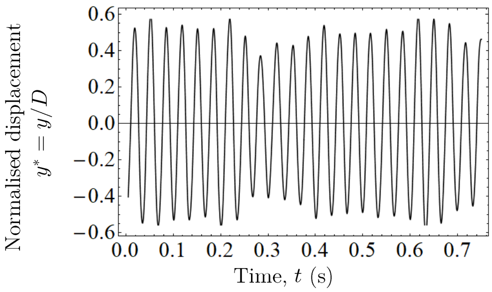

Figure 5: A sample of the time history for cylinder displacement from a test run of our experimental setup. the value of $U^* = 22.7$

3. Numerical setup validation

3.1. Simple grid independency study

Numerical solutions of actual, continuous physical phenomena contain errors, or uncertainties, due to temporal and spatial discretisation. Reliance on the numerical method of investigation puts the responsibility on the user to minimise and justify the magnitude of error introduced in the solution.

While CFD users usually point towards their low Courant-Friedrichs-Lewy number to substantiate their claim of temporal convergence for their numerical solutions, researchers demonstrate the spatial convergence of their solution through either one of these methods. First, by solving the governing equations on several grids, each grid being a finer version of the previous one and showing that the quantities of interest are approximately the constant on all grids tested. One then chooses the mesh with a medium resolution to use in the subsequent data collection (Wu, 2011; Ding et al., 2013, 2015a, 2019).

3.2. Grid independency study via Richardson extrapolation and grid convergence index

Like the first, the second method solves the governing equations on successively finer grids. However, instead of arguing that one obtains similar results on all the grids, the investigator checks whether the quantities of interest tend towards value, as one solves the governing equation on successively finer grid resolutions (Richardson and Gaunt, 1927;

Stern et al., 2001). This method, of checking for convergence pays attention not only on the presumed converged value but also on the trend of convergence. Literature that employ this method impose a monotonic convergence condition (Stern et al., 2001; Mat Ali et al., 2011; Ali et al., 2012; Maruai et al., 2018) on their quantities of interest, adding an extra layer of confidence in the final form of heir spatial discretisation.

Additionally, this method allows for a quantitative description of the degree of convergence through the grid convergence index (GCI). Let $f_1, f_2, f_3, \dots, f_n$ denote the quantity of interest obtained from several grids. A larger subscript indicates a coarser grid, this f_1 denotes the finest while f_n denotes the coarsest grid. Let the difference between successive solutions be $\epsilon_{2,1}, \epsilon_{3,2}, \epsilon_{4,3}, \dots, \epsilon_{n,n-1}$, where $\epsilon_{2,1} = f_2 - f_1$, $\epsilon_{3,2} = f_3 - f_2$ and so on. Then, the GCI is defined as

$$\mathrm{GCI}_{i+1,i} = F_s \frac{|\epsilon_{i+1,i}|}{f_i\,(r^p - 1)} \times 100\%, \tag{15}$$

where F_s, f_i and r^p denotes the safety factor ($= 1.25$), quantity of interest and the refinement ratio, r, between successive grids raised to the order of accuracu of the series of solution, p. We refer the reader to Stern et al. (2001); Langley Research Centre (2018) for a more detailed discussion on r^p.

We can estimate what the solution approaches as the grid size approaches zero by using the p$^{\text{th}}$ method. Briefly, we compute the generalised Richardson extrapolation of the quantity of interest as follows.

$$f_{\mathrm{RE}} = f_1 + \frac{f_1 - f_2}{r^p - 1}, \tag{16}$$

where f_{RE} is the Richardson extrapolation of the quantity of interest. Using f_{RE} to estimate the limit of the monotonically convergent series of f_i, we can determine the percentage difference of our solution on our finest grid from this limit as

$$E_i = \frac{f_i - f_{\mathrm{RE}}}{f_{\mathrm{RE}}} \times 100\%. \tag{17}$$

Table 2 summarises the result of our grid independency study for the SVIV reduced velocity of $U^* = 22.7$. We identified three quantities central to the investigation of fluid-structure phenomena, especially the flow-induced vibration of a circular cylinder. They are the vibration amplitude, vibration frequency and lift coefficient of the cylinder. We solve the governing equations on three grids which are numbered 1 for the finest, 2 for the medium and 3 for the

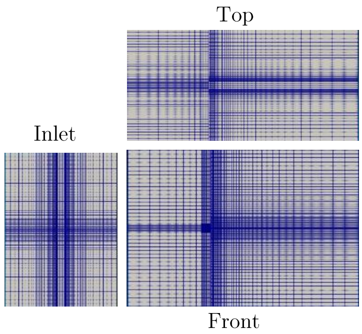

(a) Coarse

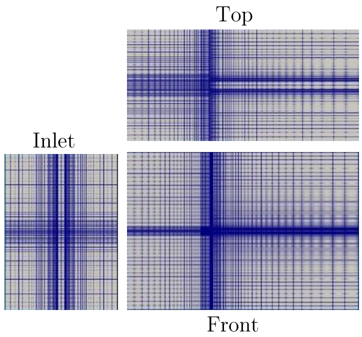

(b) Medium

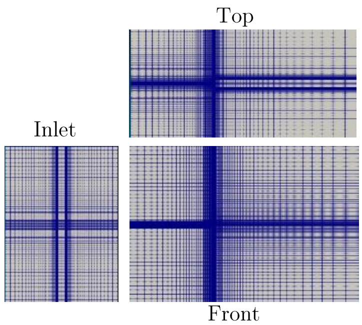

(c) Fine

Figure 6: Three meshes used in the grid convergence study. Figs. 6a, 6b and 6c show the coarse, medium and fine meshes viewed perpendicular to three main viewing positions: from the inlet, the top and the front, which is looking directly at the cylinder end.

coarsest, shown in Fig. 6. If we let v_i be the volume of the i^{th} cell in the grid, then, the average cell size is

$$h = \frac{1}{N}\left[\sum_{i=1}^{N} v_i\right]^{1/3}, \tag{18}$$

and the normalised average cell size is hence

$$h/D = \frac{1}{ND}\left[\sum_{i=1}^{N} v_i\right]^{1/3}. \tag{19}$$

Both y^*_{RMS} and Cl_{RMS} starts at an initial value smaller than their Richardson extrapolations, f_{RE}, before approaching it as we decrease the average cell size, h. This similar trend can perhaps be attributed to the causal relationship between the lift coefficient and vibration amplitude. The lift drives and sustains the vibration, hence a small lift produces a small vibration, and when the lift amplitude becomes higher, so too does the vibration amplitude. The vibration frequency, on the other hand, starts at a value larger than its f_{RE} before approaching f_{RE}.

The quantity Cl_{RMS} experiences the most significant drop in GCI as we refine the grid. The GCI is close to one-third (30.92%) as we refine the grid from coarse to medium with a refinement ratio of 1.376. The refinement ratio is calculated by dividing the number of cells in one grid with the next one down the refinement line. Following the grid numbering convention explained previously, dividing the number of cells in the fine grid (grid 1) with the number of cells in the medium grid (grid 2) gives us the refinement ratio from medium to fine, or $r_{2,1}$. Similarly, dividing the number of cells in the medium grid (grid 2) with the number of cells in the coarse grid (grid 3) gives us the refinement ratio from coarse to medium, or $r_{3,2}$. We can generalise this to $n-$number of grids as follows.

$$r_{i+1,i} = \frac{S_{\text{grid},i+1}}{S_{\text{grid},i}}, \tag{20}$$

where $S_{\text{grid},i}$ denotes the total number of cells in the i^{th} grid. The GCI of Cl_{RMS} drops further to 1.63% as the mesh is refined more with a refinement ratio of 1.304.

The GCI for y^*_{RMS} also drops by one order of magnitude as can be seen by comparing $\text{GCI}_{3,2}$ with $\text{GCI}_{2,1}$. Again, this similar trend of improvement points to the causal relationship between lift and displacement of the cylinder. The GCI for f^*, however, drops by approximately a factor of 6 instead of one order of magnitude, unlike the GCIs of y^*_{RMS} and Cl_{RMS}.

We provide visual representations of the convergent Cl_{RMS}, y^*_{RMS} and f^* series in Figs. 7, 8 and 9. Note how the quantity of interest is very close to its Richardson extrapolation at the fine grid (grid 1) for all Cl_{RMS}, y^*_{RMS} and f^*. This implies that the fine grid already provides adequate spatial discretisation for the problem we are studying, and further refinements, while able to nudge our solutions even closer to the limit that is the Richardson extrapolation, may not be optimal in terms of usage of computational resources. Values of y^*_{RMS} and f^* at the fine grid already fall within

Table 2
Summary of grid independency study.

Parameter/ metric	Cl_{RMS}	$y^*_{\text{RMS}} = y^*/D$	$f^* = f_{\text{cyl.}}/f_n$
f_{RE}	0.262	0.369	0.969
f_1	0.2598	0.3687	0.9695
f_2	0.2430	0.3588	0.9740
f_3	0.0805	0.2374	1.0220
$\lvert\epsilon_{2,1}\rvert$	0.02	0.01	0.004
$\lvert\epsilon_{2,1}\rvert$	0.16	0.12	0.48
$R = \lvert\epsilon_{2,1}\rvert / \lvert\epsilon_{2,1}\rvert$	0.10	0.08	0.094
$\text{GCI}_{3,2}$	30.92	6.00	0.64
$\text{GCI}_{3,2}$	1.63	0.52	0.10

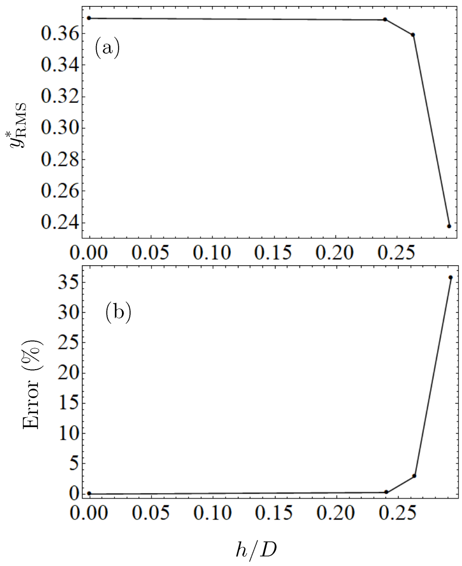

Figure 7: The convergence diagram for y^*_{RMS}. Fig. 7a shows how y^*_{RMS} converges close to the Richardson extrapolation value while Fig. 7b shows how the error (difference between the value obtained from a particular mesh and the Richardson extrapolation) decreases with decreasing grid spacing.

experimental uncertainty as evidenced by our measurement in §2.4 and the work by Koide et al. (2013). Hence, all succeeding numerical data are gathered from the fine grid.

4. Single plate amplitude and frequency response

4.1. Amplitude response

We compared our experiment and numerical results with those from Koide et al. (2013) and Nguyen et al. (2012) in Fig. 10. Figure 10a shows the amplitude response of our single plate experiment and simulation. We use the root-mean-square value of the cylinder displacement to represent the amplitude responses instead of the maximum displacement. The reason for this is twofold: first, using y^*_{RMS} facilitates comparison of data with Nguyen et al. (2012) and Koide

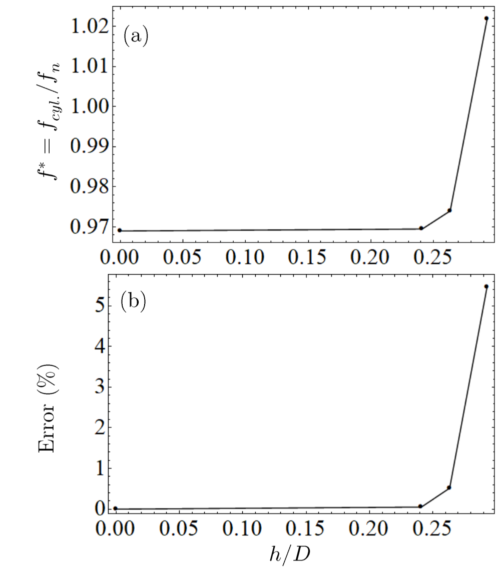

Figure 8: The convergence diagram for f^*. Fig. 8a shows how f^* convergens close to the Richardson extrapolation value while Fig. 8b shows how the error (difference between the value obtained from a particular mesh and the Richardson extrapolation) decreases with decreasing grid spacing.

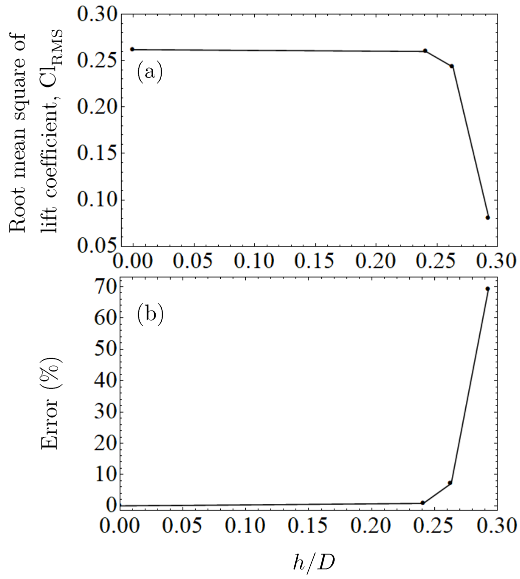

Figure 9: The convergence diagram for $\mathrm{Cl_{RMS}}$. Fig. 9a shows how $\mathrm{Cl_{RMS}}$ converges close to the Richardson extrapolation value while Fig. 9b shows how the error (difference between the value obtained from a particular mesh and the Richardson extrapolation) decreases with decreasing grid spacing.

et al. (2013), who also used y^*_{RMS} in their work. Second, because the cylinder displacement is an intermediate quantity for the estimation harnessed power (Maruai et al., 2017, 2018), the usage of root-mean-square of cylinder displacement gives a preview of mean harnessed power, once the vibration is converted into alternating current.

There is virtually no vibration for both our experiment and simulation when $U^* < 18$, except for a small peak close

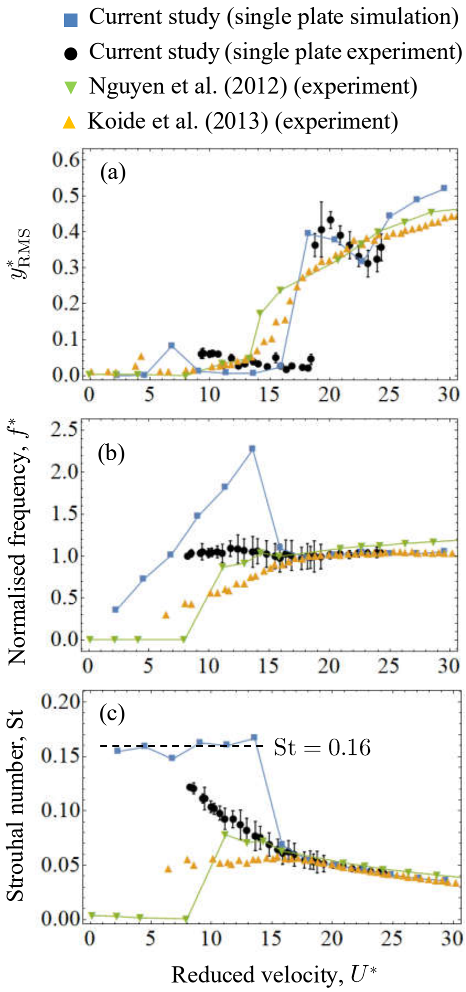

Figure 10: The amplitude and frequency response of our cruciform system, in lieu of results from Nguyen et al. (2012); Koide et al. (2013). Fig. 10a shows the amplitude response using $y^*_{\rm RMS}$, Fig. 10b the frequency response using f^* and Fig. 10c also the frequency response, but using the Strouhal number of vibration.

to 0.1 at $U^* \approx 7$. We attribute this peak to the upper branch of KVIV, which still exists, although suppressed due to the cruciform configuration of the system (Shirakashi et al., 1989; Nguyen et al., 2012). However, when U^* exceeds 18, we observe a sudden jump in U^* right up to about 0.4, for both our experiment and simulation. This we attribute to the formation of the streamwise vortices that drive SVIV.

After the inception of SVIV, the value for $y^*_{\rm RMS}$ drops down to approximately 0.3, before recovering to a value that is close to what was observed by Nguyen et al. (2012) and Koide et al. (2013). This sudden jump followed by a gradual drop and a gradual rise in $y^*_{\rm RMS}$ was not found in the works of Nguyen et al. (2012) nor Koide et al. (2013), even though their experimental parameters are reasonably close to what we use in both our experiment and simulation.

We, therefore, attribute this difference to the higher turbulence level set in our work. The turbulence level in the works of Nguyen et al. (2012), for example, was $< 2.8\%$ throughout their range of Reynolds number. Instead, the

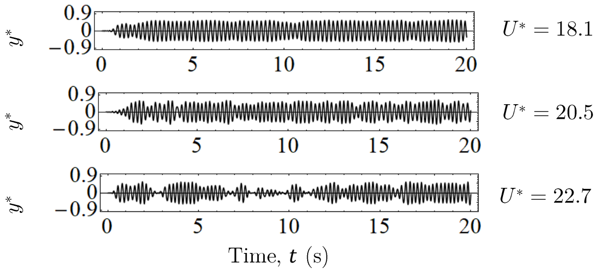

(a)

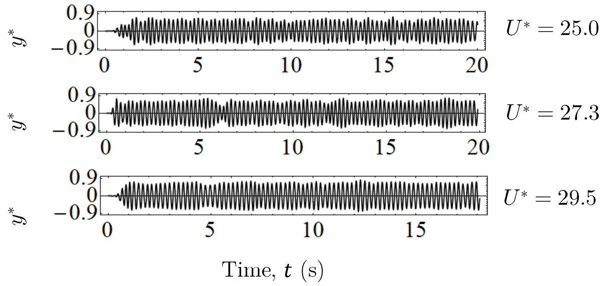

(b)

Figure 11: The time series of cylinder displacement between $18 < U^* < 20$. Fig. 11a groups the cylinder displacement signal between $18 < U^* < 23$, where there seems to be an increase in intermittency in the displacement signal, while Fig. 11b groups the cylinder displacment signal between $25 \leq U^* < 30$, where the intermittency in the displacment signal vanishes.

initial turbulence level in our setup, both experimental and numerical, is approximately double that value. Because of this, the turbulence amplification due to the onset of streamwise vortices (Zhao and Lu, 2018) — especially for a circular cylinder-strip plate cruciform (Koide et al., 2017) — is also higher compared to the experiments of Nguyen et al. (2012) and Koide et al. (2013). This higher compound turbulence warps the dominant vortical structure and introduces an increasing amount of intermittency to the lift signal, and by extension, to the displacement time history of the cylinder.

One can simply inspect the error bars within $18 < U^* < 23$ in Fig. 10a to verify the greater sample dispersion within that range of U^*. This intermittency ultimately vanishes as the dominant vortical structures become sufficiently stable to retain enough periodicity in its formation. Our numerical results also seem to support this argument, as evidenced by the time history of U^* within $18 < U^* < 30$ in Fig. 11. There exists a distinct increase in intermittency for the time histories in Fig. 11a, that disappears once $U^* > 23$ as can be seen in Fig. 11b.

We see these as grounds for further study on streamwise vortex shedding onset, perhaps from the perspective of transition from convective to absolute instability. However, such studies are more commonly done under low Reynolds number conditions (Wang et al., 2019; Li et al., 2019) to ease the isolation of the phenomenon and is therefore out of the scope of this study.

4.2. Frequency response

Figure 10b compares the frequency responses of our experiment and numerical results with those in Nguyen et al. (2012) and Koide et al. (2013). We use the normalised frequency f^* in Fig. 10b and the vibration Strouhal number in Fig. 10c to aid comparison between the results. In our experiments, the value for f^* always fall close to unity. However, if we inspect the size of the error bars, we observed a range of U^* where there exists a higher degree of variance in the sample measurements between $13 < U^* < 20$. The reason for this lies in $13 < U^* < 20$ coinciding with the desynchronization region of the KVIV regime up to $U^* < 18$, and then overlaps with the intermittent vibration regime up to $U^* < 20$. Within these two regimes, the cylinder displacement time history — from which f^* is calculated — varies considerably in amplitude and periodicity, resulting in larger error bars. In Fig. 10c we can see the overall trend being more similar to the results of Koide et al. (2013) rather than Nguyen et al. (2012), which is likely due to a higher similarity between our experimental setup with that of Koide et al. (2013), most striking in terms of the gap ratio $G = g/D$, which is the same.

Our numerical results exhibit a significantly different trend, but only up to $U^* < 17$. We observe in Fig. 10b that the vibration frequency of the cylinder increases linearly, even past $U^* = 7$, which is the upper branch of the KVIV regime. Converting f^* into Strouhal number reveals that the cylinder is vibrating close to the Karman frequency of the system. The Karman frequency of a smooth, fixed circular cylinder refers to the shedding frequency of Karman vortices in its wake. An empirical relationship with Reynolds number exists for $250 < \mathrm{Re} < 2 \times 10^5$, which is the following Blevins (1990).

$$\mathrm{St} = 0.198\left(1 - \frac{19.7}{\mathrm{Re}}\right) \tag{21}$$

The values we get using Eq. 21 are nearly constant about 0.19 for $U^* < 15$. The slight discrepancy from our Strouhal number mean (≈ 0.16) in the $U^* < 15$ range can be ascribed to us studying a cruciform structure instead of the smooth circular cylinder upon which Eq. 21 was originally based (Blevins, 1990).

The discrepancies found especially in Fig. 10b most probably stem from the same reasons explained by Nguyen et al. (2012). The lowest y^*_{RMS} recorded in our simulation within $7 < U^* < 15$ was in the order of 10^{-5} m (10 microns). A numerical study has no problem recording vibration of this order as the precision of the numerical solution is only limited by the processor architecture. Experimental work, however, requires not only the sensitivity but also the isolation from the background noise that forces the cylinder to vibrate close to the natural frequency of the system f_n (Nguyen et al., 2012), which consequently overpowers this minimal amplitude vibration. Once streamwise vortices form, however, their shedding and cylinder vibration synchronises close to f_n, thus locking the normalised vibration frequency back to $f^* \approx 1$.

5. Temporal evolution of the lift coefficient

Alternating lift drives the cylinder vibration during VIV. Despite this central position in determining the temporal stability of the amplitude and frequency responses, most studies in the SVIV literature dealt with the lift (coefficient) as if it is only a function of flow velocity, U or reduced velocity, U^* (Kawabata et al., 2013; Koide et al., 2013; Hemsuwan et al., 2018). We believe that parties interested in the quality of power harnessed from flow around a cruciform should give similar attention to the transient nature of SVIV as they did for the global characteristics of the flow such as the root mean squares of cylinder displacement, lift coefficient, and dominant frequency through fast Fourier transform (FFT). We think that this is especially the case for the lift signal, to better gauge the room for improvement in future iterations of the system.

5.1. Ensemble empirical mode decomposition and Hilbert transform

To obtain a clearer picture of the temporal characteristics of the lift and cylinder displacement signals, we decided to employ the ensemble empirical mode decomposition (EEMD) method (Huang et al., 1998; Wu and Huang, 2008) on the signals, and compute their instantaneous phase lag, frequency and amplitude using the Hilbert transform.

The Hilbert transform (HT) has been used in the past to study the instantaneous phase and frequencies of KVIV (Khalak and Williamson, 1999). However, the signal must be monochromatic if we are to obtain a physically meaningful result after applying HT. EEMD is a way to pre-process the signal and get components that (1) have zero mean, and (2) have an equal number of extrema and zero crossings, or they differ only by one. Functions that fulfil these criteria are called intrinsic mode functions (IMF), and they guarantee a physically meaningful result to HT (Gumelar et al., 2019; Zhou et al., 2019). Unlike Fourier transform, which is an analytical method of signal decomposition based on circular functions in the complex plane, EEMD is algorithmic, and the processes undertaken can be summarised as follows.

Produce 150 white noise signals of length equal to the original signal and amplitude equal to 0.2 of the standard deviation of the original signal. Then, add to the set of white noises the original signal – creating 150 variations of the original signal. Following that, we apply the empirical mode decomposition (EMD) algorithm on each of the 150 signals. The EMD algorithm is summarised below.

1. Construct the envelope of the signal by connecting all maxima/minima with cubic splines.
2. Find the local mean of the envelope for the span of the data.
3. Find the difference between the local mean and the original data.
4. Repeat steps 1 and 2 on the difference in 3 for ten times (Wu and Huang, 2008).

The steps above produce a set of intrinsic mode functions or IMFs for each of the 150 variations of the original signal. Then, we average the first IMF component from each of the decomposed original signal variations, to obtain the first EEMD IMF C_1 of the original signal. We do the same for the second, third, until the n^{th} component for each of the 150 original signal variations, thus obtaining $C_2, C_3, \ldots, C_n$.

To compute the phase lag between lift coefficient Cl and normalised cylinder displacement y^*, we select the component with the highest correlation to the original signal, to represent the original signal. The phase lag, instantaneous frequency, and instantaneous amplitude of the original signal is subsequently computed by taking the constructing an analitical signal $z(t)$ from $C_1, C_2, \ldots, C_n$ by computing the Hilbert transform of the IMF, H_i,

$$H_i(t) = \frac{1}{\pi}\mathrm{PV}\int^{\infty} \frac{C_i(\tau)}{t-\tau}d\tau, \tag{22}$$

where PV denotes the Cauchy principal value, and then constructing the analitical signal as follows.

$$z(t) = C_i(t) + iH_i(t) \tag{23}$$

Note that i in Eq. 23 is the complex number.

We refer the reader interested in the details of EEMD and Hilbert transform, also collectively known as the Hilbert-Huang transform (HHT), to the following excellent texts on the subject (Huang and Attoh-Okine, 2005; Huang, 2014).

5.2. Phase lag in the KVIV regime ($U^* < 14$)

At reduced velocities $U^* = 2.3$ and 4.5, the phase lags ϕ (deg.) between Cl and U^* are practically zero. The characteristic IMFs of Cl and y^* at $U^* = 4.5$ exemplifies this trend, as showcased in Fig. 12. The characteristic IMFs are the EEMD components of Cl and y^* that has the highest correlation with the original y^* signal. The trend that one notices in Fig. 12 is similar to what was observed in Khalak and Williamson (1999), a study that also employs the Hilbert transform to obtain the instantaneous phase, albeit without EEMD. Both Cl and y^* are in phase with each other and the normalised dominant frequency of the lift coefficient $f^*_{\mathrm{Cl}} = f_{\mathrm{Cl}}/f_n$ (Fig. 12c) falls about one quarter short of the system natural frequency f_n.

Once we enter the upper branch of KVIV at $U^* = 6.8$, ϕ jumps to approximately 110 deg. This jump in ϕ is characteristic of the transition to the upper branches as also observed by Maruai et al. (2018), among others. Both Cl and y^* signals are visibly very periodic, and the dominant frequency of Cl, i.e. f^*_{Cl}, is ≈ 1, as one can verify in Fig. 13c.

As we increase U^* even further up to $U^* < 14$, we see a similar trend for all $U^* = 9.1, 11.4, 13.6$ examined: the

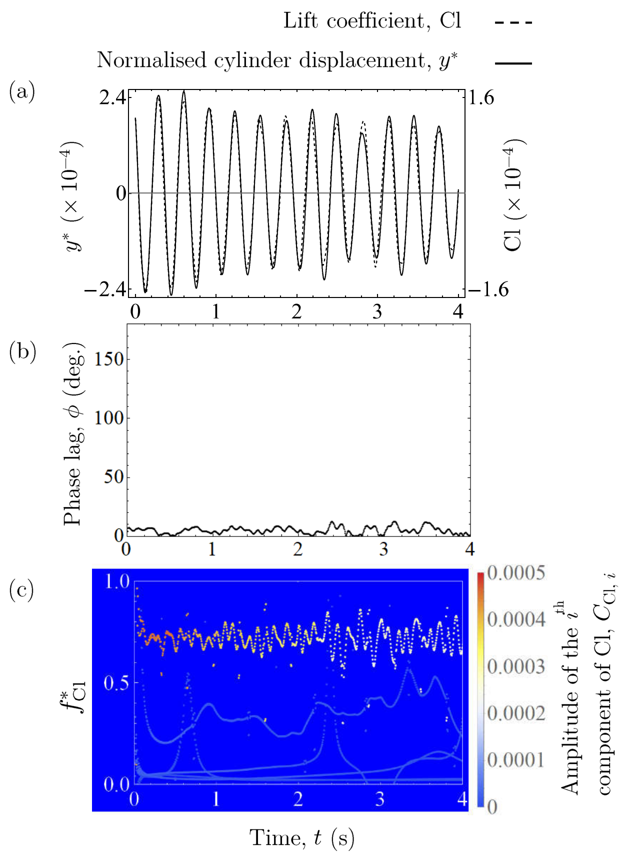

Figure 12: Temporal analysis of the lift coefficient and normalised cylinder displacement signal at $U^* = 4.5$. We show the lift coefficient and normalised cylinder displacement signal side by side in Fig. 12a, present the temporal evolution of the phase lag ϕ of Cl in Fig. 12b and show the temporal evolution of the instantaneous frequency of the lift coefficient signal in Fig. 12c. The blue line in Fig. 12a represents the lift coefficient signal, while the black line represents the normalised cylinder displacement.

signal of Cl and y^* are both qualitatively very periodic, the phase lag is very close to 180 deg., and the dominant Cl frequency increases linearly in a manner that the Strouhal number of Cl is always ≈ 0.16 on average. We present a sample of the (1) Cl and y^* signals, (2) ϕ, and (3) f^*_{Cl} in the $6.8 < U^* < 14$ range in Figs. 14a, 14b and 14c respectively. The sample is taken from the numerical results at $U^* = 13.6$, and it is characteristic of a KVIV system in the lower branch.

5.3. Transition to SVIV ($15.9 < U^* < 18.2$)

Previously in the $U^* < 14$ regime, we observed that the temporal profile of both Cl and y^* are very similar to each other, except that Cl leads y^* by a certain amount. This similarity in profile supports the assertion that the vibration within $U^* < 14$ is driven exclusively by the shedding of Karman vortices, which brings the onset of the alternating lift. By extension, one might expect a similar profile between Cl and y^* even when streamwise vortices drive the vibration. However, this does not seem to be the case.

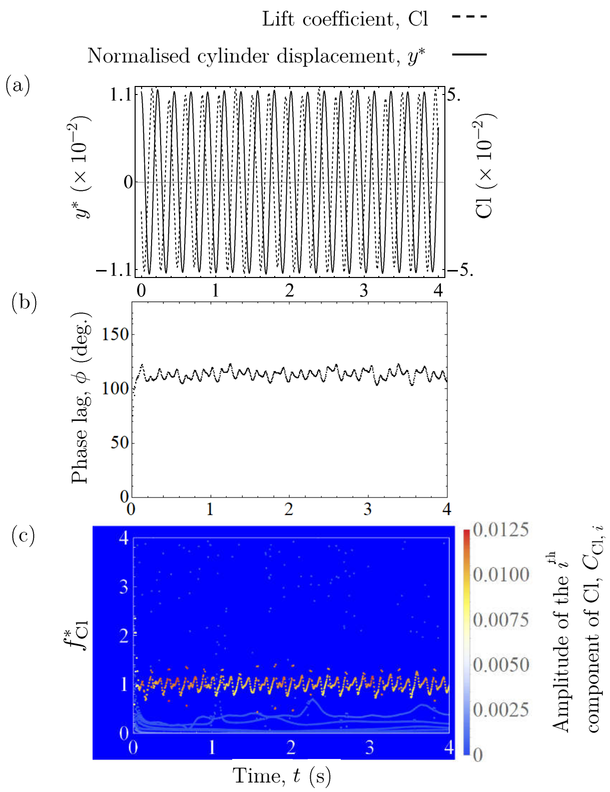

Figure 13: Temporal analysis of the lift coefficient and normalised cylinder displacement signal at $U^* = 6.8$. We show the lift coefficient and normalised cylinder displacement signal side by side in Fig. 13a, present the temporal evolution of the phase lag ϕ of Cl in Fig. 13b and show the temporal evolution of the instantaneous frequency of the lift coefficient signal in Fig. 13c. The blue line in Fig. 13a represents the lift coefficient signal, while the black line represents the normalised cylinder displacement.

Once we reach $U^* = 15.9$, we observe that it has become difficult to argue that the profile of y^* is just a lagged version of the profile of Cl. This is shown in Fig. 15a, with the enlarged version in Fig. 15b. The profile of Cl looks like the result of several superimposed signals, which one can almost distinguish from the presence of two types of maxima at two different amplitude heights. We put a red dashed line and a red dashed-dot line in Fig. 15b as visual cues indicating the two amplitude heights. Decomposing the lift coefficient signal using EEMD reveals partial evidence supporting the superimposed (compound) signal hypothesis.

Once we have decomposed the signal using EEMD, we replot Fig. 15a using the component of Cl with the highest correlation to the original y^* signal and present the comparison in Fig. 16a. To represent y^* in Fig. 16a, we again chose its IMF component with the highest correlation to the original y^* signal, as we have done in Figs. 12, 13, and 14. One can clearly see that the part of Cl signal responsible for driving the vibration at $U^* = 15.9$ is embedded in the original Cl signal, and decomposition via EEMD managed to recover this signal whose profile is indeed similar to the profile of the characteristic IMF of y^*, except that it leads y^* on average by approximately 150 deg. (Fig. 16b). This decline from $\phi \approx 180$ deg. at reduced velocities $6.8 < U^* < 14$, to $\phi \approx 150$ deg. at $U^* = 15.9$ is quite sizeable,

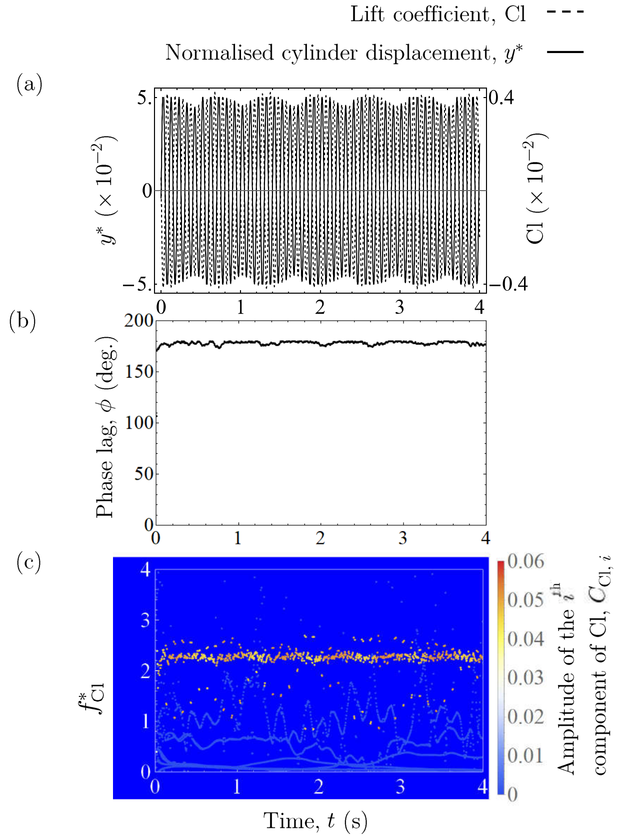

Figure 14: Temporal analysis of the lift coefficient and normalised cylinder displacment signal at $U^* = 13.6$. We show the lift coefficient and normalised cylinder displacment signal side by side in Fig. 14a, present the temporal evolution of the phase lag ϕ of Cl in Fig. 14b and show the temporal evolution of the instantaneous frequency of the lift coefficient signal in Fig. 14c. The blue line in Fig. 14a represents the lift coefficient signal, while the black line represents the normalised cylinder displacement.

suggesting a fundamental change in flow dynamics, particularly in terms of vortical structure.

Inspecting the HHT spectrogram in Fig. 16c reveals two dominant bands in the frequency domain. The first one, marked with a white continuous rectangular box, is the instantaneous frequency for the IMF component of lift shown in Fig. 16a, and its mean frequency lies close to the natural frequency of the system ($f^*_{\mathrm{Cl}} \approx 1$). There is; however, a second band of the frequency with nearly similar amplitude around $f^*_{\mathrm{Cl}} \approx 3.3$, marked with a white dashed rectangular box. Computing the Strouhal number from this frequency returns a value of $\mathrm{St} = 0.20$, which is very close to the Strouhal number for Karman vortices as predicted by Eq. 21 at the Reynolds number equivalent to $U^* = 15.9$, which is $\mathrm{Re} = 7.9 \times 10^3$. We thus attribute this second band of frequency as being the footprint left by the shedding of Karman vortices, and the first band as the result of streamwise vortex shedding.

The knowledge that Karman vortices continue to exist and shed from a cruciform structure during SVIV is not new in the literature. However, this is the first time the lift signal from a cruciform structure undergoing SVIV has been subjected to EEMD, revealing the signature of the two dominant vortical structures regulating the flow around

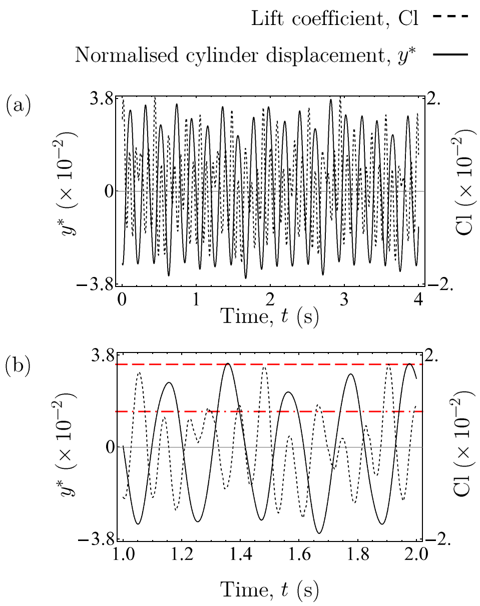

Figure 15: Temporal evolution of y^* and Cl at $U^*15.9$. Fig. 15b shows an enlarged view of Fig. 15a. We can barely spot semblance of two signals with different amplitudes superimposed in the Cl signal in Fig. 15b.

the cruciform. Although the magnitude of the instantaneous frequency due to Karman vortex is comparable to the streamwise vortex (sometimes even bigger), the reason why the cylinder resists locking into its frequency is perhaps that its frequency too distant from the natural frequency of the system f_n. The shedding frequency of the streamwise vortex is much closer to f_n and is thus preferred by the cylinder.

We consider the transition to SVIV to be complete at $U^* = 18.2$, when the mean phase lag ϕ drops further to ≈ 20 deg. Figure 17a and 17b documents this observation. The phase lag is observed to slip through 360 deg. At certain portions of the characteristic Cl profile where there are slight distortions in the periodicity of the IMF. The slipping through 360 deg. was also observed by Khalak and Williamson (1999) in their work on KVIV, which highlights the quasi-periodic nature of the signal being analysed. There, the slip appeared in Khalak and Williamson (1999) at the initial branch of KVIV. It may be the case that the overall low value of $\phi \approx 20$ deg. at $U^* = 18.2$, coupled with the presence of ϕ slippage is suggesting the possibility of $U^* = 18.2$ being the initial branch for SVIV. We could not foresee this point brought up if the original Cl signal is not decomposed beforehand, implying the utility of EEMD in studying fluid-structure interactions with multiple dominant flow structures.

5.4. The stable SVIV regime ($U^* > 20$)

As U^* is increased to 20.5, we can see a jump in ϕ from a mean value of approximately 20 deg. to about 120 deg., shown in Fig. 18a. The phase slippage discussed previously is also observed in this time series subset, indicating the quasi-periodic nature of the lift coefficient signal at this U^*. Incidentally, this quasi-periodicity seems to be the norm

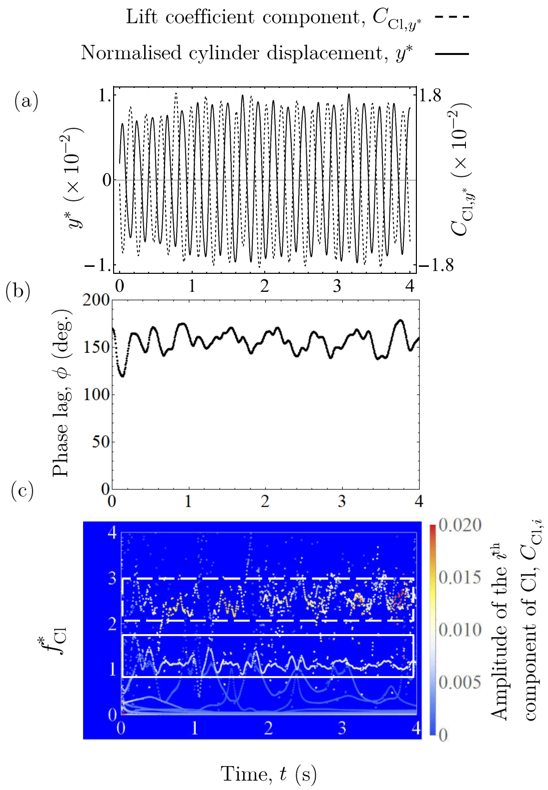

Figure 16: Temporal analysis of the lift component that has the highest correlation to the original (normalised) cylinder displacment signal, C_{Cl,y^*}, and the normalised cylinder displacement signal at $U^* = 15.9$. The component was obtained by decomposing the lift coefficient signal using EEMD. We show C_{Cl,y^*} and y^* signal side by side in Fig. 16a, present the temporal evolution of the phase lag ϕ of C_{Cl,y^*} in Fig. 16b and show the temporal ecolution of the instantaneous frequency of the C_{Cl,y^*} in Fig. 16c. The blue line in Fig. 16c represents the lift coefficient component signal, while the black line represents the normalised cylinder displacement.

for the lift signals up to $U^* = 27.3$, as suggested by the phase slippages evident in Figs. 17b, c and d. The slippage only stops once U^* reaches 29.5, suggesting a more periodic behaviour of the lift coefficient compared to its counterparts between $20.5 \leq U^* \leq 27.3$. Although the instantaneous phase between $20.5 \leq U^* \leq 27.3$ implies a quasi-periodic nature, their mean values at each U^* are contained in the narrow region $114 < \phi$ (deg.) < 135, as is the value for ϕ at $U^* = 29.5$. This observation that the value of ϕ is only slowly varying with respect to U^*, once U^* increases past 20.5, can be interpreted as the dominant flow structures settling into a stable form that becomes more resilient against external excitations. Based on this feature, it seems appropriate to classify $20.5 \leq U^* \leq 29.5$ as the upper branch of SVIV.

Figure 19 summarises our findings thus far, with respect to our analysis of the Cl time series, specifically the ensemble average value of ϕ, denoted as ϕ_{mean}. The region an indicates the initial branch of KVIV, where ϕ_{mean} is close to zero. Region B denotes the upper/lower branch of KVIV, where the system experiences a jump from $\phi_{\mathrm{mean}} \approx 0$ to greater than 110 deg. The value of ϕ_{mean} settles very close to 180 deg. towards the end of this upper/lower branch.

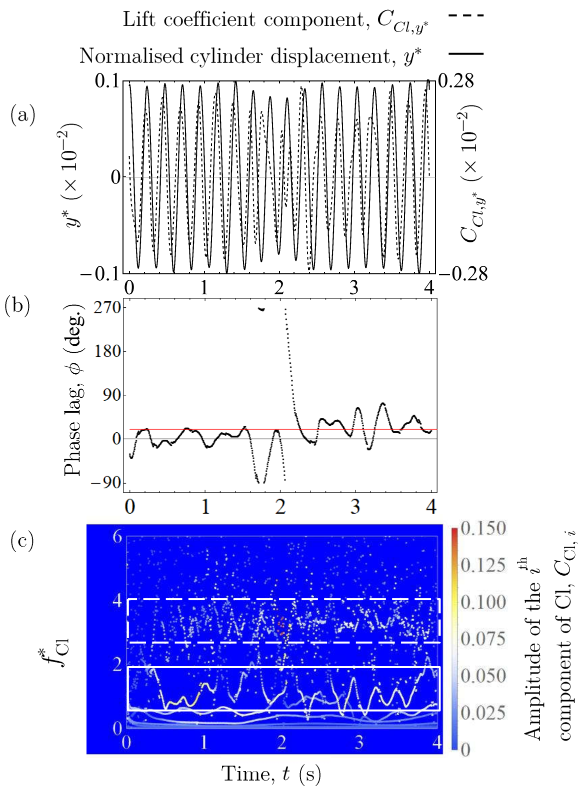

Figure 17: Temporal analysis of the lift coefficient component that has the highest correlation to the original (normalised) cylinder displacement signal, C_{Cl,y^*}, and the normalised cylinder displacement signal at $U^* = 18.2$. The component was obtained by decomposing the lift coefficient signal using EEMD. We show C_{Cl,y^*} and y^* side by side in Fig. 17a, present the temporal evolution of the phase lag ϕ of C_{Cl,y^*} in Fig. 17b and show the temporal evolution of the instantaneous frequency of the C_{Cl,y^*} in Fig. 17c. The blue line in Fig. 17a represents the lift coefficient component signal, while the black line represents the normalised cylinder displacement.

The HHT spectrograms up to this U^* show only one dominant band of f^*_{Cl} which is close to the Strouhal frequency of Karman vortex shedding.

Then, ϕ_{mean} experiences a slight drop of about one-sixth the value of ϕ_{mean} at the preceding upper/lower branch as we enter region C, marking the start of the transition to the SVIV regime. The emergence of two dominant instantaneous frequency bands for f^*_{Cl} further supports this demarcation. One of the dominant f^*_{Cl} band has a value close to unity, and the other has a value close to the shedding frequency of Karman vortex for a fixed, isolated circular cylinder at the same Reynolds number. The system then undergoes a more sudden drop to $\phi_{\mathrm{mean}} \approx 20$ deg. at $U^* = 18.2$. Inspecting the temporal evolution of ϕ revealed the quasi-periodic nature of Cl at this U^*, which is analogous to the KVIV initial branch studied by Khalak and Williamson (1999), prompting us to assign the region up to $U^* = 20.5$ as the initial branch of SVIV (region D).

Finally, in region E, we observe another jump in ϕ_{mean} from $\phi_{\mathrm{mean}} \approx 20$ deg. to approximately 120 deg. as $U^* > 20.5$. The Cl signal gradually loses its quasi-periodicity with increasing U^*, and the ϕ_{mean} in this region falls

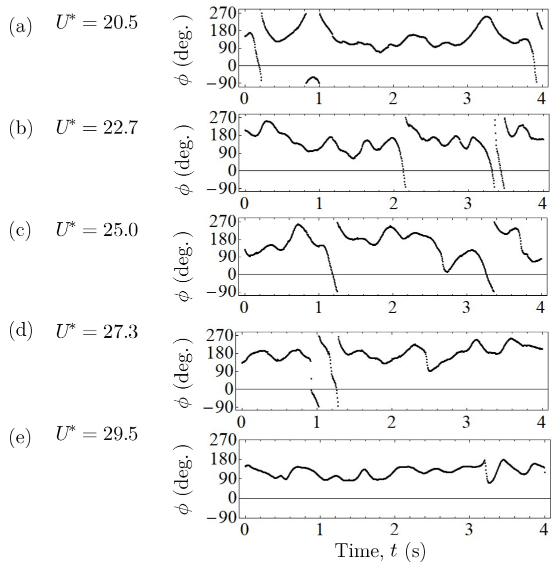

Figure 18: The instantaneous phase lag ϕ of the dominant component of the normalised cylinder displacement signal (y^*) against C_{Cl,y^*} in the range $20 < U^* < 30$. See Fig. 17 for the definition of C_{Cl,y^*}.

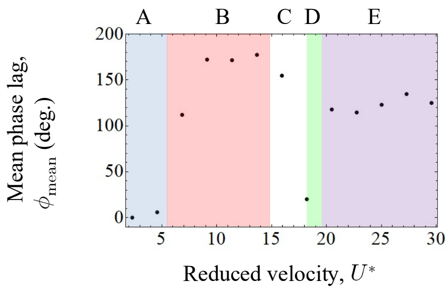

Figure 19: Vibration regimes identified during analyss of ϕ. To capture the evolution of ϕ with respect to U^*, a representative value for ϕ at each U^* must be selected. We chose to use the mean ϕ as the representative value.

within the arguably narrow range of $114 < \phi$ (deg.) < 135, pointing to stabilisation of dominant flow structures. We hence designate region E as the upper branch of SVIV.

6. Estimation of harnessable power

6.1. Mathematical model for power estimation

The mathematical model for harnessable power estimation in this study follows that which had been derived in Raghavan et al. (2007). In these works, the authors mentioned that work done by the oscillating cylinder $W_{\mathrm{cyl.}}$ during one cycle of oscillation $T_{\text{osc.}}$ is as follows.

$$W_{\text{cyl.}} = \int_0^{T_{\text{osc.}}} \left(F_{\text{L}} \cdot \dot{y}\right) dt \tag{24}$$

where both the lift F_{L} and cylinder velocity $\dot{y}$ are both functions of time. Through several manipulations and simplifying assumptions (Sun et al., 2016), the power captured by the system can be written, using our parameters, as the fluid power

$$P_{\text{Fluid,RMS}} = \frac{1}{2}\rho\pi C_{\text{Cl,RMS}} U^2 f_{\text{cyl.}} y^*_{\text{RMS}} D L \sin(\phi), \tag{25}$$

or the mechanical power

$$P_{\text{Mech.,RMS}} = 8\pi^3 m_{\text{eff.}} \zeta_{tot.} \left(y^*_{\text{RMS}} f_{\text{cyl.}}\right)^2 f_n. \tag{26}$$

Here, $P_{\text{Fluid,RMS}}$, $P_{\text{Mech.,RMS}}$, L, $C_{\text{Cl,RMS}}$, $\zeta_{tot.}$ and $m_{\text{eff.}}$ are the root mean square of fluid power, root mean square of mechanical power, length of the circular cylinder, characteristic root mean square of lift amplitude, total damping coefficient, and the system effective mass respectively. We choose to use root mean square (parameters with subscript RMS) quantities in Eq. 24 instead of the maximum values like the original authors because that may lead to a misunderstanding that the maximum value is sustained throughout the observation window. This obviously is not always the case in our study, especially once the flow transits to SVIV. Time series analysis of $y^*(t)$ and $\text{Cl}(t)$ in §4.1 revealed that there is a degree of intermittency in both signals that cannot be overlooked at specific ranges of U^*, thus making it better to use the root mean square values instead. Estimation of the root mean square of harnessable power in our opinion makes more sense because it returns a value that is continually approached by the system *over time*, while the maximum, could be a one-off value.

Before presenting the results of our harnessable power estimation following Eqs. 25 and 26, let us clarify our method of estimating the root mean square of lift amplitude $C_{\text{Cl,RMS}}$. Let $F_{\text{L}}(t)$ be the lift acting on the cylinder and $y(t)$ the cylinder displacement time series resulting from that alternating lift. Decomposing $F_{\text{L}}(t)$ via EEMD yields a finite number N of IMFs which we can summarily write as $F_L(t) = \sum^{N} C_i(t)$. The IMF chosen as the component of lift driving $y(t)$ is the $C_i(t)$ with the highest correlation with $y(t)$, i.e. the component due to streamwise vortex. We then compute the root mean square value of that component of lift, giving us $C_{\text{Cl,RMS}}$.

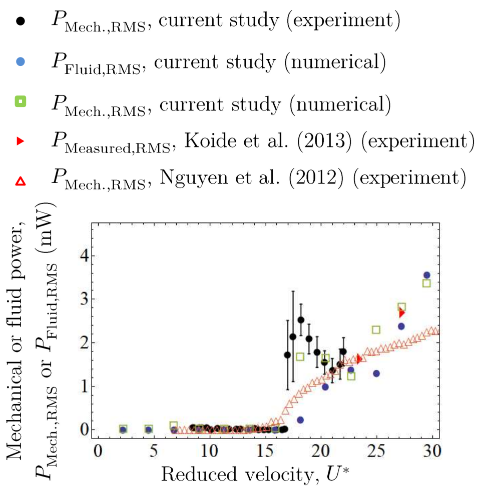

Figure 20: Estimated root mean square of mechanical power $P_{\mathrm{Mech.,RMS}}$, fluid power $P_{\mathrm{Fluid,RMS}}$, or both, of our experimental and numerical results, compared with results of similar studies in the literature. The fluid power $P_{\mathrm{Fluid,RMS}}$ is calculated only from the results of our numerical study as the others did not measure lift. The computation of the instantaneous phase lag ϕ requires both lift and cylinder displacement signals.

Figure 20 shows the comparison between power estimated from our experiment and numerical results, with the experimental results of Nguyen et al. (2012) and the direct power measurement of Koide et al. (2013). Only the value for $P_{\mathrm{Mech.,RMS}}$ is computed from our experimental results due to the absence of lift data. Our numerical results have both lift and cylinder displacement data, and hence, we calculated both $P_{\mathrm{Fluid,RMS}}$ and $P_{\mathrm{Mech.,RMS}}$. We estimated the power from the experimental results of Nguyen et al. (2012) by interpolating missing data points in both their amplitude and frequency responses to compute the value of $P_{\mathrm{Mech.,RMS}}$ at a given value of U^*. The direct power measurement by Koide et al. (2013) was done by connecting the elastic support of the cylinder to a coil. The coil moves with the cylinder, thus creating a relative pistoning motion against a fixed magnet and produces an alternating current.

We note that the evolution trend of estimated power with respect to U^* is similar between $P_{\mathrm{Mech.,RMS}}$ from our experiment and simulation, especially in the U^* region immediately after the onset of SVIV. This makes sense since $P_{\mathrm{Mech.,RMS}}$ is basically a single variable function, the variable being y^*_{RMS}, with the others fixed as we vary U^*. The trend observed in $P_{\mathrm{Mech.,RMS}}$ is thus a scaled version of the trend found in y^*_{RMS}. Nevertheless, besides this region of $18 < U^* < 23$ the trend between all data series compared in Fig. 21 are relatively similar. This trend is especially the case after $U^* > 23$, where we observe a fairly good agreement between $P_{\mathrm{Mech.,RMS}}$ and $P_{\mathrm{Fluid,RMS}}$ computed from our experimental and numerical results with the direct power measurements of Koide et al. (2013) and the estimated $P_{\mathrm{Mech.,RMS}}$ from the data of Nguyen et al. (2012). The estimated power in the KVIV regime $U^* < 17$ produces power only in the order of µW, which is relatively insignificant in contrast to the magnitude of power produced in the SVIV regime (mW).

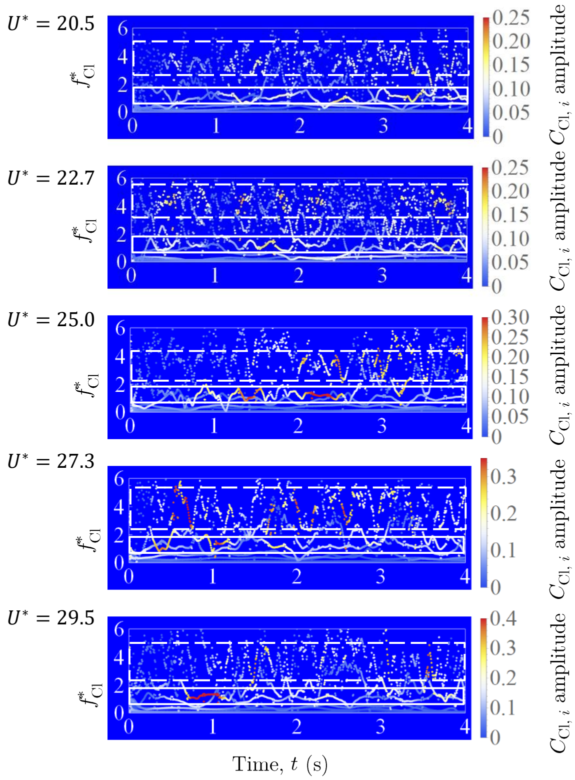

Figure 21: The instantaneous frequency of the lift signal between $20 < U^* < 30$. The white, solid box encloses the region where the mean frequency is close to the system natural frequency f_n, while the dashed, white box encloses the region where the mean frequency is close to the shedding frequency of Karman vortex at the Reynolds number at which at the simulation is performed. Through visual inspection, we can see how the degree of dispersion in the instantaneous frequency of the "Karman component" of lift is about twice that of the "streamwise component" of lift.

6.2. Possibility for increasing fluid power, $P_{\mathrm{Fluid,RMS}}$

We have seen in Fig. 20 the similarity in the evolution trend of $P_{\mathrm{Mech.,RMS}}$ and $P_{\mathrm{Fluid,RMS}}$ against U^* of our numerical results with those from Nguyen et al. (2012) and Koide et al. (2013). However, recall that to represent the amplitude of lift, we used the root mean square amplitude of the component of lift that has the highest correlation with the original cylinder displacement signal $y(t)$. We did not use the root mean square amplitude of the original lift signal, and yet we obtained $P_{\mathrm{Fluid,RMS}}$ estimates that are in reasonable agreement not only with its $P_{\mathrm{Mech.,RMS}}$ counterparts but with the actual measured power of Koide et al. (2013).

On the one hand, this is an indication that the lift component selected for use in computation is an arguably faithful representation of the force driving the motion of the cylinder. The fact that it is a reasonably good representation also suggests that the motion of the cylinder, once it enters the SVIV regime, is driven only by a component, and not the totality of the lift force. Another significant subset of the lift force is the component whose mean frequency is close to the Karman frequency of vortex shedding, as explained in §5.3. This Karman component of lift has a similar order of magnitude to the streamwise component of lift, as evidenced in Fig. 21, and is therefore not negligible. The Karman

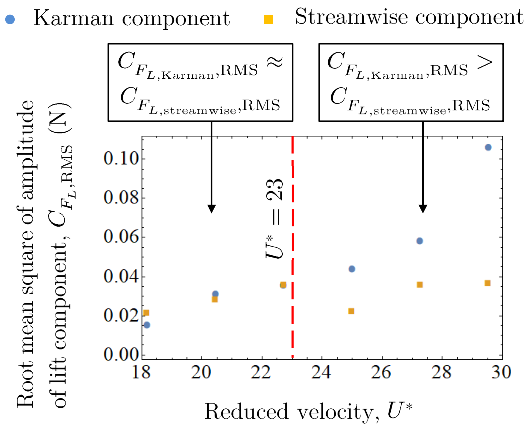

Figure 22: Evolution of the root mean square amplitude of two dominant lift components, Karman and streamwise vortices with respect to U^*. The region $U^* < 23$ exhibits similar magnitude for both the Karman and streamwise components of lift. On the other hand, the magnitude of amplitude for the Karman component while the region $U^* > 23$ is almost always twice that of the streamwise component.

components are marked with a dashed, white box, and the streamwise components are marked with a solid, white box, following the convention in Figs. 12, 13, 14, 16 and 17. However, the Karman component fails to affect the cylinder vibration like the streamwise component most probably due to the large difference between the mean frequency of the Karman component and the natural frequency of the system, f_n. The streamwise component has a mean frequency close to f_n and is hence able to synchronise with the vibration of the cylinder, producing a sizeable amplitude response.

Figure 22 shows the root-mean-square amplitude of the Karman and streamwise components of lift in the SVIV regime $U^* > 18$. Between $18 < U^* < 23$, the magnitude of the Karman and streamwise components are nearly equal. However, once we exceed $U^* = 23$, Fig. 22 shows that the contribution to the root-mean-square amplitude of total lift by the Karman component is on average twice the contribution of the streamwise component. Let us assume a hypothetical situation where we can transfer the contribution by the Karman component to the streamwise component of lift. Then, the value for $C_{\text{Cl,RMS}}$ in Eq. 25 will increase close to a factor of 2 when $18 < U^* < 23$, and close to a factor of 3 when $23 < U^* < 30$. This increase in $C_{\text{Cl,RMS}}$ will lead to a larger $P_{\text{Fluid,RMS}}$, if the value of the other parameters in Eq. 25 are similar. This exercise demonstrates the room for improvement possible for $P_{\text{Fluid,RMS}}$ in future developments of cruciform energy harvesters.

7. Conclusions

In this study, we numerically investigated the temporal evolution of the lift coefficient and cylinder displacement signals of an elastically supported cruciform system in the range $1.1 \times 10^3 < \text{Re} < 14.6 \times 10^3$, or $2.3 < U^* < 29.5$. Our circular cylinder diameter is 10 mm and the natural frequency of the system is 4.4 Hz. Validation of key numerical results was made experimentally in a custom-built open flow channel, using a cruciform system whose parameters were tuned as close as possible to the quantities used in the numerical study.

We observed the amplitude response to reach large magnitudes when the dominant frequency of lift is close to the natural frequency of the system, i.e. f_n. This observation explains the maxima in the amplitude response at $U^* = 6.8$, which takes place at the upper branch of the KVIV regime, i.e. $2.3 \leq U^* 13.6$. The onset of streamwise vortex shedding imposes an additional degree of complexity on the lift coefficient signal, causing it to deviate from the sinusoidal-like signature of lift observable in the KVIV regime. This complexity is, however, not observed in the cylinder displacement signal, which remains relatively similar to a sinusoidal function. Decomposing the lift coefficient signal in the SVIV regime ($15.9 \leq U^* \leq 29.5$) using EEMD allows us to see that the complexity of the lift coefficient signal as probably being caused by the superimposition of two dominant components of lift. One due to the shedding of Karman and the other due to the shedding of streamwise vortices. This component of lift has a mean frequency close to f_n. Through visual inspection, it is relatively similar to a sinusoidal function. This sinusoidal profile results in a similar pattern in the cylinder displacement signal in the SVIV regime.

Application of the Hilbert-Huang transform on the most dominant component of cylinder displacement – and the component of lift most correlated to it – allows for the computation of the instantaneous phase lag between lift and cylinder displacement. The temporal mean of the instantaneous phase lag revealed five "branches" of vibration, among which is the initial branch of SVIV at $U^* = 18.2$, which has never been identified before in the literature.

Estimation of power from our results show that the root-mean-square mechanical and fluid power computed from our numerical work to be in fairly good agreement with the root-mean-square mechanical power computed from our experiments. There are, however, discrepancies with the trend found in other literature, especially within $15.9 \leq U^* \leq 20.5$, which is right after the onset of SVIV. These discrepancies are probably due to deviations from the literature in terms of the fluid environment we subject the cruciform system to during data collection (open flow channel v.s. water tunnel, medium flow turbulence v.s. low flow turbulence). Finally, we estimated the upper limit for improvement of the root-mean-square fluid/mechanical power and found that the root-mean-square powers can potentially be increased close to a factor of 2 within $18 < U^* < 23$ and close to a factor of 3 when $23 < U^* < 30$. We base the estimation on the ability to minimise the contribution from Karman vortices, while maximising the contribution from streamwise vortices towards the total root-mean-square lift amplitude.

References

Ali, M.S.M., Doolan, C.J., Wheatley, V., 2012. Low Reynolds number flow over a square cylinder with a detached flat plate. International Journal of Heat and Fluid Flow 36, 133–141. URL: http://dx.doi.org/10.1016/j.ijheatfluidflow.2012.03.011, doi:10.1016/j.ijheatfluidflow.2012.03.011.

Bernitsas, M., Raghavan, K., 2008. Reduction/suppression of VIV of circular cylinders through roughness distribution at $8 \times 10^3 < \mathrm{Re} < 1.5 \times 10^5$, in: Proceedings of the International Conference on Offshore Mechanics and Arctic Engineering - OMAE.

Bernitsas, M.M., Ben-Simon, Y., Raghavan, K., Garcia, E.M.H., 2009. The VIVACE Converter: Model Tests at High Damping and Reynolds Number Around 10^5. Journal of Offshore Mechanics and Arctic Engineering 131. URL: http://offshoremechanics.asmedigitalcollection.asme.org/article.aspx?articleid=1472649, doi:10.1115/1.2979796.

Bernitsas, M.M., Raghavan, K., Ben-Simon, Y., Garcia, E.M.H., 2008. VIVACE (Vortex Induced Vibration Aquatic Clean Energy): A New Concept in Generation of Clean and Renewable Energy From Fluid Flow. Journal of Offshore Mechanics and Arctic Engineering 130, 041101. URL: http://www.scopus.com/record/display.url?eid=2-s2.0-56749179917{&}origin=resultslist{&}sort=plf-f{&}src=s{&}st1=A+new+concept+in+generation+of+clean+and+renewable+energy+from+fluid+flow{&}sid=620865A71FAF26768C42655E1E8BC194.aXczxbyuHHiXgaIW6Ho7g:230{&}sot=b{&}sdt=b{&}h, doi:10.1115/1.2957913.

Blevins, R.D., 1990. Flow-induced vibration .

Deng, J., Ren, A.L., Shao, X.M., 2007. The flow between a stationary cylinder and a downstream elastic cylinder in cruciform arrangement. Journal of Fluids and Structures 23, 715–731. URL: https://www.sciencedirect.com/science/article/pii/S0889974606001472, doi:10.1016/J.JFLUIDSTRUCTS.2006.11.005.

Ding, L., Bernitsas, M.M., Kim, E.S., 2013. 2-D URANS vs. experiments of flow induced motions of two circular cylinders in tandem with passive turbulence control for 30,000. Ocean Engineering 72, 429–440. URL: http://www.sciencedirect.com/science/article/pii/S0029801813002448?via{%}3Dihub, doi:10.1016/J.OCEANENG.2013.06.005.

Ding, L., Zhang, L., Kim, E.S., Bernitsas, M.M., 2015a. URANS vs. experiments of flow induced motions of multiple circular cylinders with passive turbulence control. Journal of Fluids and Structures 54, 612–628. doi:10.1016/j.jfluidstructs.2015.01.003.

Ding, L., Zhang, L., Wu, C., Mao, X., Jiang, D., 2015b. Flow induced motion and energy harvesting of bluff bodies with different cross sections. Energy Conversion and Management doi:10.1016/j.enconman.2014.12.039.

Ding, W., Sun, H., Xu, W., Bernitsas, M.M., 2019. Numerical investigation on interactive FIO of two-tandem cylinders for hydrokinetic energy harnessing. Ocean Engineering 187, 106215. URL: https://www.sciencedirect.com/science/article/pii/S0029801819304019, doi:10.1016/J.OCEANENG.2019.106215.

Gumelar, A.B., Purnomo, M.H., Yuniarno, E.M., Sugiarto, I., 2019. Spectral Analysis of Familiar Human Voice Based On Hilbert-Huang Transform, in: 2018 International Conference on Computer Engineering, Network and Intelligent Multimedia, CENIM 2018 - Proceeding. doi:10.1109/CENIM.2018.8710943.

Hemsuwan, W., Sakamoto, K., Takahashi, T., 2018. Numerical investigation of lift-force generation on a moving circular cylinder in a uniform flow driven by longitudinal vortex. Journal of Fluids and Structures 83, 448–470. URL: https://www.sciencedirect.com/science/article/pii/S0889974617308885, doi:10.1016/J.JFLUIDSTRUCTS.2018.09.010.

Huang, N.E., 2014. Hilbert-Huang transform and its applications. volume 16. World Scientific.

Huang, N.E., Attoh-Okine, N.O., 2005. The Hilbert-Huang transform in engineering. CRC Press.

Huang, N.E., Shen, Z., Long, S.R., Wu, M.C., Snin, H.H., Zheng, Q., Yen, N.C., Tung, C.C., Liu, H.H., 1998. The empirical mode decomposition and the Hubert spectrum for nonlinear and non-stationary time series analysis. Proceedings of the Royal Society A: Mathematical, Physical and Engineering Sciences doi:10.1098/rspa.1998.0193.

Kawabata, Y., Takahashi, T., Haginoya, T., Shirakashi, M., 2013. Interference Effect of Downstream Strip-Plate on the Crossflow Vibration of a Square Cylinder. Journal of Fluid Science and Technology 8, 647–658. doi:10.1299/jfst.8.348.

Khalak, A., Williamson, C., 1999. Motions, Forces And Mode Transitions In Vortex-Induced Vibrations At Low Mass-Damping. Journal of Fluids and Structures 13, 813–851. URL: http://www.sciencedirect.com/science/article/pii/S0889974699902360, doi:10.1006/jfls.1999.0236.

Koide, M., Kato, N., Yamada, S., Kawabata, Y., Takahashi, T., Shirakashi, M., 2007. Influence Of A Cruciform Arrangement Downstream Strip-Plate On Crossflow Vibration. Journal of Computational and Applied Mechanics 8, 135–148.

Koide, M., Ootani, K., Yamada, S., Takahashi, T., Shirakashi, M., 2006. Vortex Excitation Caused by Longitudinal Vortices Shedding from Cruciform Cylinder System in Water Flow. JSME International Journal 49, 1043–1048.

Koide, M., Sekizaki, T., Yamada, S., Takahashi, T., Shirakashi, M., 2009. A Novel Technique for Hydroelectricity Utilizing Vortex Induced Vibration, in: Proceedings of the ASME Pressure Vessels and Piping Division Conference, PVP2009-77487.

Koide, M., Sekizaki, T., Yamada, S., Takahashi, T., Shirakashi, M., 2013. Prospect of Micro Power Generation Utilizing VIV in Small Stream Based on Verification Experiments of Power Generation in Water Tunnel. Journal of Fluid Science and Technology 8, 294–308. URL: https://www.jstage.jst.go.jp/article/jfst/8/3/8{_}294/{_}articlehttp://jlc.jst.go.jp/DN/JST.JSTAGE/jfst/8.294?lang=en{&}from=CrossRef{&}type=abstract, doi:10.1299/jfst.8.294.

Koide, M., Takahashi, T., Shirakashi, M., Salim, S.A.Z.B.S., 2017. Three-dimensional structure of longitudinal vortices shedding from cruciform two-cylinder systems with different geometries. Journal of Visualization , 1–11.

Langley Research Centre, 2018. Turbulence Modeling Resource. URL: https://turbmodels.larc.nasa.gov/.

Li, X., Lyu, Z., Kou, J., Zhang, W., 2019. Mode competition in galloping of a square cylinder at low Reynolds number. Journal of Fluid Mechanics 867, 516–555. URL: https://www.cambridge.org/core/product/identifier/S0022112019001605/type/journal{_}article, doi:10.1017/jfm.2019.160.

Maruai, N.M., Ali, M.S.M., Ismail, M.H., Zaki, S.A., 2018. Flow-induced vibration of a square cylinder and downstream flat plate associated with micro-scale energy harvester. Journal of Wind Engineering and Industrial Aerodynamics 175, 264–282. URL: https://www.scopus.com/inward/record.uri?eid=2-s2.0-85042219159{&}doi=10.1016{%}2Fj.jweia.2018.01.010{&}partnerID=40{&}md5=2f3f62b94bb69ced3368b32e682aefc7, doi:10.1016/j.jweia.2018.01.010.

Maruai, N.M., Mat Ali, M.S., Ismail, M.H., Shaikh Salim, S.A.Z., 2017. Downstream flat plate as the flow-induced vibration enhancer for energy harvesting. Journal of Vibration and Control , 107754631770787URL: http://journals.sagepub.com/doi/10.1177/1077546317707877, doi:10.1177/1077546317707877.

Mat Ali, M.S., Doolan, C.J., Wheatley, V., 2011. Low Reynolds number flow over a square cylinder with a splitter plate. Physics of Fluids 23. doi:10.1063/1.3563619.

Nguyen, T., Koide, M., Yamada, S., Takahashi, T., Shirakashi, M., 2012. Influence of mass and damping ratios on VIVs of a cylinder with a downstream counterpart in cruciform arrangement. Journal of Fluids and Structures 28, 40–55. doi:10.1016/j.jfluidstructs.2011.10.006.

Raghavan, K., 2007. Energy Extraction from a Steady Flow Using Vortex Induced Vibration. Doctoral dissertation. The University of Michigan. URL: http://deepblue.lib.umich.edu/handle/2027.42/55687.

Raghavan, U., Albert, R., Kumara, S., 2007. Near linear time algorithm to detect community structures in large-scale networks. Phys. Rev E. 76, 036106.

Richardson, L.F., Gaunt, J.A., 1927. The deferred approach to the limit. Philosophical Transactions of the Royal Society A doi:https://doi.org/10.1098/rsta.1927.0008.

Shirakashi, M., Mizuguchi, K., Bae, H.M., 1989. Flow-induced excitation of an elastically-supported cylinder caused by another located downstream in cruciform arrangement. Journal of Fluids and Structures 3, 595–607. doi:10.1016/S0889-9746(89)90150-3.

Stern, F., Wilson, R.V., Coleman, H.W., Paterson, E.G., 2001. Comprehensive approach to verification and validation of CFD simulationsï£¡part 1: methodology and procedures. Journal of fluids engineering 123, 793–802.

Sun, H., Kim, E.S., Nowakowski, G., Mauer, E., Bernitsas, M.M., 2016. Effect of mass-ratio, damping, and stiffness on optimal hydrokinetic energy conversion of a single, rough cylinder in flow induced motions. Renewable Energy 99, 936–959. URL: http://www.sciencedirect.com/science/article/pii/S0960148116306206, doi:10.1016/j.renene.2016.07.024.

Wang, S., Wen, F., Shi, X., Zhou, X., 2019. Stability analysis of asymmetric wakes. Physics of Fluids doi:10.1063/1.5098111.

Wu, W., 2011. Two-Dimensional RANS Simulation of Flow Induced Motion of Circular Cylinder with Passive Turbulence Control. Doctoral dissertation. The University of Michigan.

Wu, Z., Huang, N.E., 2008. Ensemble Empirical Mode Decomposition: A Noise-Assisted Data Analysis Method. Advances in Adaptive Data Analysis doi:10.1142/s1793536909000047.

Zhang, B., Mao, Z., Song, B., Ding, W., Tian, W., 2018. Numerical investigation on effect of damping-ratio and mass-ratio on energy harnessing of a square cylinder in FIM. Energy 144, 218–231. URL: https://www.scopus.com/inward/record.uri?eid=2-s2.0-85037995662{&}doi=10.1016{%}2Fj.energy.2017.11.153{&}partnerID=40{&}md5=01db7c6b6d4d44e88de7045843c7d423, doi:10.1016/j.energy.2017.11.153.

Zhao, M., Lu, L., 2018. Numerical simulation of flow past two circular cylinders in cruciform arrangement. Journal of Fluid Mechanics 848, 1013–1039. URL: https://www.cambridge.org/core/product/identifier/S0022112018003804/type/journal{_}article, doi:10.1017/jfm.2018.380.

Zhou, L., Meng, Y., Abbaspour, K.C., 2019. A new framework for multi-site stochastic rainfall generator based on empirical orthogonal function analysis and Hilbert-Huang transform. Journal of Hydrology doi:10.1016/j.jhydrol.2019.05.047.